

# Adaptive Output-Feedback Image-Based Visual Servoing for Quadrotor Unmanned Aerial Vehicles

Hui Xie<sup>1</sup>, Alan F. Lynch<sup>2</sup>, *Member, IEEE*, Kin Huat Low, and Shixin Mao

**Abstract**—This brief presents an adaptive output feedback image-based visual servoing (IBVS) law for a quadrotor unmanned aerial vehicle. The control objective is to regulate the relative 3-D position and yaw of the vehicle to a planar horizontal visual target consisting of multiple points. The control is implemented using a minimal number of commonly available low-cost on-board sensors including a strapdown inertial measurement unit and a monocular camera. The IBVS method relies on moment image features which are defined using a virtual camera. Output feedback introduces a filter to the control which removes the common requirement for linear velocity measurement. The method is adaptive and compensates for a constant force disturbance appearing the translational dynamics and parameter uncertainty in thrust constant, desired feature depth, and mass. Exponential stability of the outer loop and combined inner–outer closed-loop error dynamics is proven. Flight tests demonstrate the proposed method’s motion control performance and its ability to compensate parametric uncertainty and reject constant force disturbances.

**Index Terms**—Image-based visual servoing (IBVS), output-feedback control, unmanned aerial vehicles (UAVs).

## I. INTRODUCTION

CURRENTLY, there is a strong interest in computer vision systems mounted on-board unmanned aerial vehicles (UAVs) to provide passive, inexpensive, and lightweight sensing of the environment. Adding vision improves the autonomy of the vehicle, e.g., ego-motion estimation and planning can be performed in areas where GPS is unavailable [1], [2]. Vision can be integrated into the closed-loop motion control of the vehicle, and this is referred to as *visual servoing*. Visual servoing is usually categorized into two approaches:

position-based visual servoing (PBVS) and image-based visual servoing (IBVS) [3]. This brief focuses on IBVS where the error signal to be stabilized is defined in the image plane. Unlike PBVS, IBVS avoids pose reconstruction which requires accurate camera calibration and a prior 3-D model of the target. In general, IBVS is simpler to implement and relatively insensitive to camera calibration error [4]. The control objective considered in this brief is to regulate the relative 3-D position and yaw between the vehicle and a horizontal planar target consisting of multiple points. We choose an IBVS approach for a quadrotor UAV with a single on-board downward-facing camera. Traditionally, IBVS for fixed-base manipulator robots is developed using image feature kinematics [3]. However, the dynamics of a robot should be considered for high-speed tasks or when the system is underactuated [5]. We consider a traditional quadrotor which is underactuated, and the IBVS law presented directly accounts for its dynamics. In addition, a primary focus of this brief is to eliminate the need for linear velocity measurement, and this requires the UAV dynamics to be included in the control design. An IBVS law based on a robot’s dynamics is referred to as a *dynamic IBVS* [6].

Work [6] categorizes existing dynamic IBVS methods for underactuated UAVs into four groups: the spherical image moment-based design [7], [8], the homography-based method [9], [10], the virtual spring approach [11], [12], and the virtual camera approach [13], [14]. Other than the virtual spring approach which is based on an output feedback design, the work mentioned earlier assumes linear velocity measurement. To avoid this assumption, some IBVS designs use optical flow. For example, [15] and [16] use spherical image moment features from [7] and optical flow to estimate a scaled linear velocity. A nonlinear adaptive control design is proposed to ensure global asymptotic stability (GAS) of the outer closed loop. In [17], spherical optical flow and an attitude estimate are combined to estimate scaled linear velocity. A GAS adaptive controller is applied to landing on a moving a platform. Instead of requiring additional sensors or software to compute optical flow, some approaches use output feedback. Work in [18] and [19] uses spherical image moment features and an observer to estimate linear velocity. Both simulation and experimental results show the observer’s robustness to unknown depth information. However, a robustness analysis is not provided. In [20], spherical image moment features are adopted and an adaptive output feedback backstepping controller is used for IBVS. Although a GAS result is provided for the outer loop, this brief is not experimentally validated.

Manuscript received August 16, 2018; accepted December 25, 2018. Date of publication January 28, 2019; date of current version April 13, 2020. Manuscript received in final form January 5, 2019. This work was supported in part by the National Science Foundation of China under Grant 51705086 and in part by the Traffic Management of Unmanned Aerial Systems Project under Grant NTU-ATMRI 2016-D3-LOW. Recommended by Associate Editor G. Hu. (*Corresponding author: Shixin Mao.*)

H. Xie is with the School of Computing, Engineering and Mathematics, Western Sydney University, Penrith, NSW 2751, Australia (e-mail: hui.xie@westernsydney.edu.au).

A. F. Lynch is with the Department of Electrical and Computer Engineering, University of Alberta, Edmonton, AB T6G 1H9, Canada (e-mail: alan.lynch@ualberta.ca).

K. H. Low is with the School of Mechanical and Aerospace Engineering, Nanyang Technological University, Singapore 639798 (e-mail: mkhlow@ntu.edu.sg).

S. Mao is with the School of Mechanical and Aerospace Engineering, Nanyang Technological University, Singapore 63978, and also with the Nanjing University of Aeronautics and Astronautics Shenzhen Institute, Shenzhen 518057, China (e-mail: maosx618@126.com).

Color versions of one or more of the figures in this article are available online at <http://ieeexplore.ieee.org>.

Digital Object Identifier 10.1109/TCST.2019.2892034

Recently, attention has focused on output feedback methods with moment features using a virtual camera. Moment features originate from [21] and have a simple decoupled image feature kinematics which facilitates controller design. Work in [22] uses image moments of points viewed in a virtual camera with zero roll and pitch relative to the visual target plane but whose yaw motion follows the real camera. A uniformly ultimately bounded output feedback IBVS law is proposed using the image moment as state coordinates. Work in [22] is one of the few known papers which analyze the stability of the moving target case with no assumptions made about the target motion. Other work [23] presents an observer-based backstepping controller with the same virtual camera as in [22]. The depth of the desired image is assumed known *a priori*. Experimental results show the performance of the proposed approach. In [24], an output feedback backstepping controller with the image moment features from a virtual camera defined in [22] is developed. This approach is adaptive to uncertainties in thrust constant and attitude bias which have a noticeable effect on UAV motion and create steady-state error [6]. Alternatively, in [25], the image moment features and a virtual camera with no rotational motion are used. As in [23], the desired image depth is assumed known and only asymptotic stability is proven.

Using the virtual camera and image moment features in [22]–[24], this brief proposes a novel output feedback control. As mentioned earlier, output feedback eliminates the need for linear velocity measurement. Relative to [24], the proposed method improves the stability property of the closed-loop from asymptotically stable (AS) to exponentially stable (ES). ES is important as it ensures bounded tracking error for moving targets. Another contribution is to provide ES in the presence of constant force disturbances entering the translational dynamics and to compensate for parametric uncertainty in thrust constant, mass, and desired depth. Taking desired image depth as unknown makes the method more broadly applicable compared to [23] and [25]. Estimating desired depth is inconvenient and requires reconstruction which assumes known target geometry and intrinsic camera parameters. Robustness to constant force disturbance, thrust constant, and mass is not present in [22], [23], and [25]. Flight tests are an important component of this brief and validate the performance of the proposed control. This should be compared to the related work [22], [25] where only simulations are provided. The modified PX4 autopilot source has been released to the community to promote further collaborative development.

This brief is organized as follows. Section II describes the system modeling. Section III presents the output feedback-based IBVS control. Experimental results are in Section IV, and concluding remarks are in Section V.

## II. DYNAMIC IBVS MODELING

In this section, we present a summary of the open-loop modeling of the UAV and vision system. More details can be found in [6]. As shown in Fig. 1, the visual target considered in this brief lies in a horizontal plane and is composed of  $N > 1$  coplanar feature points. A navigation frame  $\mathcal{N}$  is

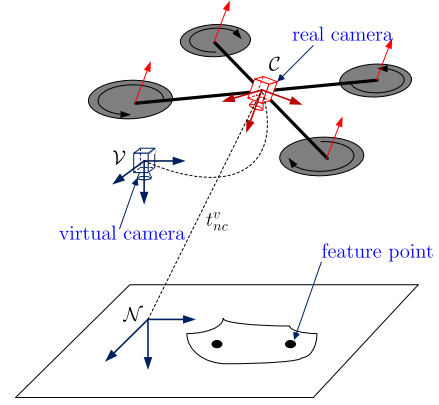


Fig. 1. Definition of reference frames. Although  $\mathcal{V}$  and  $\mathcal{C}$  share the same origin, for clarity they are shown with a position offset.

assumed to be inertial and fixed to a point on the Earth. As mentioned in Section I, a virtual camera with zero roll and pitch is employed to define image features for visual servoing. To describe the IBVS modeling, a virtual camera frame  $\mathcal{V}$  and a real camera frame  $\mathcal{C}$  are introduced with their origin attached to the optical center of the real camera. Expressed in  $\mathcal{N}$ , the displacement from the origin of  $\mathcal{N}$  to the origin of  $\mathcal{C}$  is denoted  $t_{nc}^v = [t_1, t_2, t_3]^T$ . As in [6], we use the point image moment feature denoted by vector  $s = [s_l^T, s_h, s_\psi]^T$ , where  $s_l \in \mathbb{R}^2$ . Then, the dynamic IBVS model can be written as

$$\dot{s}_l = -\lambda v_l / Z^{v*} - S s_l \dot{\psi} \quad (1a)$$

$$\dot{s}_h = -v_3^v / Z^{v*} \quad (1b)$$

$$\dot{s}_\psi = -\dot{\psi} \quad (1c)$$

$$\dot{v}^v = -[\dot{\psi} E_3]_\times v^v + g E_3 - (F^v + \Delta) / m \quad (1d)$$

$$\dot{R} = R[\omega^c]_\times \quad (1e)$$

$$\dot{\omega}^c = -J^{-1}[\omega^c]_\times J \omega^c + J^{-1} \tau^c \quad (1f)$$

where  $\lambda$  is the focal length of the camera;  $Z^{v*}$  is the desired depth of the target plane in  $\mathcal{V}$ ;  $g$  is the gravity constant;  $m$  is the mass of the vehicle;  $J$  is the inertia of the vehicle;  $E_3 = [0, 0, 1]^T$ ; the orientation between  $\mathcal{N}$  and  $\mathcal{C}$  is denoted by  $R \in \text{SO}(3)$  and parameterized by the Euler angles  $\eta = [\phi, \theta, \psi]^T$ , with  $\phi$  denoting roll,  $\theta$  pitch, and  $\psi$  yaw; the vector  $v^v = [v_l^T, v_3^v]^T = [v_1^v, v_2^v, v_3^v]^T$  is the linear velocity of the camera expressed in  $\mathcal{V}$ ;  $\omega^c$  is the angular velocity of the camera in  $\mathcal{C}$ ;  $S = \begin{bmatrix} 0 & -1 \\ 1 & 0 \end{bmatrix}$ ;  $[x]_\times y = x \times y$ ;  $\Delta = [\Delta_1, \Delta_2, \Delta_3]^T$  is an unknown disturbance force;  $F^v = -R_{\theta\phi} E_3 T_M$ ;  $T_M = K_T u_h$  is the total thrust;  $K_T$  is the thrust constant and the rotation  $R_{\theta\phi}$  is  $R$  with zero yaw;  $\tau^c = M_\tau \bar{\tau}^c$  is the moment created by the propellers; and  $M_\tau = \text{diag}\{K_T l / (2\sqrt{2}), K_T l / (2\sqrt{2}), K_\tau\}$  where  $l$  is the arm length and  $K_\tau$  is the counter torque constant. Although these force and torque models are approximate, they are commonly used [26]. The normalized inputs  $u_h$  and  $\bar{\tau}^c$  for (1a) can be expressed as

$$\begin{bmatrix} u_h \\ \bar{\tau}^c \end{bmatrix} = \frac{1}{2} \begin{bmatrix} \frac{1}{2} & \frac{1}{2} & \frac{1}{2} & \frac{1}{2} \\ -1 & 1 & 1 & -1 \\ 1 & -1 & 1 & -1 \\ -1 & -1 & 1 & 1 \end{bmatrix} \begin{bmatrix} \tilde{W}_1^2 \\ \tilde{W}_2^2 \\ \tilde{W}_3^2 \\ \tilde{W}_4^2 \end{bmatrix}$$

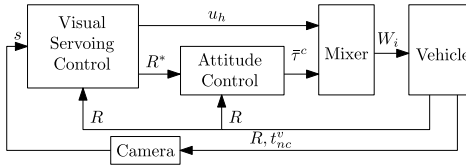


Fig. 2. Dynamic visual servoing with an inner-outer control loop structure.

where  $\tilde{W}_i$  is the normalized pulsewidth given by  $\tilde{W}_i = (W_i - W_{\min}) / (W_{\max} - W_{\min})$ ,  $W_i$  is the pulsewidth modulation signal to the electronic speed controller (ESC) driving the  $i$ th motor,  $W_{\min}$  and  $W_{\max}$  are the minimum and maximum usable values, respectively. From the definition of  $u_h$  and  $\bar{\tau}^c$ , it can be shown that  $u_h \in [0, 1]$  and  $\bar{\tau}_i^c \in [-1, 1]$ ,  $i = 1, 2, 3$

$$F^v = -K_T u_h [c_\phi s_\theta, -s_\phi, c_\phi c_\theta] \approx K_T u_h [-\theta, \phi, -1] \quad (2)$$

where  $s_* = \sin(*)$  and  $c_* = \cos(*)$ . We remark this small angle approximation is not necessary and can be removed to prove outer loop stability in a straightforward manner. However, we take the approximation for a number of reasons. First, in practice, roll and pitch are small and the linear approximation is sufficient to obtain good performance. The low-cost camera used on the experimental platform has a small field of view (FoV) and small roll and pitch ensure the target remains in its FoV. Second, it simplifies the discussion regarding the entire (i.e., inner and outer) closed-loop stability. Most of the papers mentioned in Section I do not take a small roll and pitch approximation in the stability analysis of the outer loop. However, they do not perform an entire closed-loop analysis. An exception is [25] which considers the stability analysis of the entire closed loop. However, this last work does not provide experimental validation or the same robustness to uncertainty and force disturbance as the proposed method.

As confirmed in [6], a constant bias in the measurement of  $\phi$  and  $\theta$ , and the variation in thrust constant  $K_T$  results in nonzero steady-state image feature error. In this brief, the effect of measurement error in  $\phi$  and  $\theta$  is included in disturbance  $\Delta$  in (1d). The disturbance can also include other effects such as wind gusts. As in [17], disturbance  $\Delta$  is assumed constant. The control objective is to regulate the image feature  $s$  to its desired value  $s^*$  while being robust to additive disturbance  $\Delta$  and uncertainty in  $K_T$ ,  $m$ , and  $Z^{v*}$ .

### III. DYNAMIC IBVS CONTROL

#### A. Two-Loop Structure

As in [6] and shown in Fig. 2, we adopt a cascade two-loop control structure. To regulate the image feature error to zero, the outer IBVS loop takes the image feature  $s$  as input and provides attitude reference  $R^*$  to the inner loop and normalized thrust  $u_h$  to the Mixer. The inner attitude loop tracks the reference  $R^*$  from the outer IBVS loop by outputting a normalized torque  $\bar{\tau}^c$  to the Mixer. The normalized signals  $u_h$ ,  $\bar{\tau}^c$  pass through the Mixer to determine the ESC inputs  $W_i$ . The justification and benefits of choosing this structure are given in [6]. In this brief, the high bandwidth of the inner attitude loop is achieved by a proportional-integral-derivative (PID) controller. As mentioned earlier, unlike [6], the outer

IBVS loop does not require a measurement of linear velocity since an output feedback design is employed.

#### B. Output Feedback Dynamic IBVS Control

Based on (1b), (1d), and (2), the height subsystem is written as

$$\dot{s}_h = -v_3^v / Z^{v*} \quad (3a)$$

$$\dot{v}_3^v = g - (K_T u_h - \Delta_3) / m \quad (3b)$$

where  $u_h$  is the input for subsystem (3). When the vehicle hovers at the desired height, the image feature  $s_h = 1$ . Hence, the objective for the height subsystem is to regulate the image feature error  $e_{sh} = s_h - 1$  to zero. Inspired by the work in [27], where an output feedback control law was developed to control the motion of robot arms, the control law for the height subsystem is designed as

$$u_h = k_h(\vartheta_{h2} - \vartheta_{h1}) + \hat{C}_g + C_{g0} \quad (4)$$

with  $\vartheta_{h1} = \dot{e}_{sh} + \alpha_h e_{sh}$ ,  $\vartheta_{h2} = \dot{\tilde{e}}_{sh} + l_{hd} \tilde{e}_{sh}$ ,  $\tilde{e}_{sh} = e_{sh} - \hat{e}_{sh}$  and

$$\dot{\hat{e}}_{sh} = -\hat{v}_h + l_h \tilde{e}_{sh} \quad (5a)$$

$$\dot{\hat{v}}_h = -l_{hd} l_h \tilde{e}_{sh} \quad (5b)$$

$$\dot{\hat{C}}_g = -\gamma_h(\vartheta_{h1} + \vartheta_{h2}) \quad (5c)$$

where  $\alpha_h$ ,  $k_h$ ,  $l_h$ ,  $l_{hd}$ , and  $\gamma_h$  are the positive control gains;  $\hat{e}_{sh}$  is the estimate of  $e_{sh}$ ;  $\hat{v}_h$  is the estimate of  $v_3^v / Z^{v*}$ ;  $C_{g0}$  is a constant estimate of  $C_g = (mg + \Delta_3) / K_T$  which is the thrust input to compensate gravity and  $\Delta_3$ ; and  $\hat{C}_g$  is the estimate of  $C_g - C_{g0}$ . We note that although  $\vartheta_{h1}$  and  $\vartheta_{h2}$  are not directly measured, using (5a), the control (4) can be written in terms of measured variables as

$$u_h = k_h(\hat{v}_h + (l_{hd} - l_h)\tilde{e}_{sh} - \alpha_h e_{sh}) + C_{g0} - \gamma_h(e_{sh} + \tilde{e}_{sh}) - \gamma_h \int_0^t (\alpha_h e_{sh} + l_{hd} \tilde{e}_{sh}) d\zeta. \quad (6)$$

From (1a), (1d), and (2), the lateral subsystem is

$$\dot{s}_l = -\lambda v_l / Z^{v*} - S s_l \dot{\psi} \quad (7a)$$

$$\dot{v}_l = K_T u_h S \eta_1 / m - S v_l \dot{\psi} + \Delta_{12} \quad (7b)$$

where  $\eta_1 = [\phi, \theta]^T$  is the input to subsystem (7), and  $\Delta_{12} = [\Delta_1, \Delta_2]^T$ . Without loss of generality, the desired value of  $s_l$  is taken as zero, i.e., the image feature error is  $e_{sl} = s_l$ . Similar to the height subsystem, the desired value of  $\eta_1$  denoted by  $\eta_1^* = [\phi^*, \theta^*]^T$  is chosen as

$$\eta_1^* = k_l S(\vartheta_{l2} - \vartheta_{l1}) + S \hat{\Delta}_l \quad (8)$$

with  $\vartheta_{l1} = \dot{e}_{sl} + \alpha_l e_{sl}$ ,  $\vartheta_{l2} = \dot{\tilde{e}}_{sl} + l_{ld} \tilde{e}_{sl}$ ,  $\tilde{e}_{sl} = e_{sl} - \hat{e}_{sl}$  and

$$\dot{\hat{e}}_{sl} = -\hat{v}_l + l_l \tilde{e}_{sl} \quad (9a)$$

$$\dot{\hat{v}}_l = -l_{ld} l_l \tilde{e}_{sl} \quad (9b)$$

$$\dot{\hat{\Delta}}_l = -\gamma_l(\vartheta_{l1} + \vartheta_{l2}) \quad (9c)$$

where  $\alpha_l$ ,  $k_l$ ,  $l_l$ ,  $l_{ld}$ , and  $\gamma_l$  are the positive control gains,  $\hat{\Delta}_l$  is the estimate of  $\Delta_l = m \Delta_{12} / K_T$  and its initial value is chosen as zero. The control law (8) can be expressed in



terms of known states  $e_{sl}$ ,  $\hat{e}_{sl}$ , and  $\hat{v}_{sl}$ . As in [6], to make  $s_\psi$  exponentially converge to zero, the yaw reference is taken as

$$\psi^* = k_\psi \int_0^t s_\psi(\xi) d\xi, \quad k_\psi > 0. \quad (10)$$

*Theorem 1:* Consider system (1c), (3), and (7), where  $\Delta$  is an unknown constant disturbance, and parameters  $Z^{v*}$ ,  $K_T$ , and  $m$  are unknown constants. The equilibrium  $[s_h - 1, v_3^v, s_l, v_l, s_\psi]^T = 0$  of the closed loop with control (4), (8), and (10) is ES if positive control gains satisfy

$$\begin{aligned} b_h k_h - \alpha_h &> 0, \quad l_h - l_{hd} - b_h k_h > 0 \\ b_l k_l - \alpha_l &> 0, \quad l_l - l_{ld} - b_l k_l > 0 \end{aligned} \quad (11)$$

where  $b_h = K_T/(mZ^{v*})$ ,  $b_l = \lambda K_T C_g/(mZ^{v*})$ , and we assume  $\eta$  tracks  $\eta^* = [(\eta_1^*)^T, \psi^*]^T$  perfectly, i.e.,  $\eta_1 = \eta_1^*$  and  $\psi = \psi^*$ .

*Proof:* Using kinematics (1c) and control (10), the closed-loop system for yaw is ES

$$\dot{s}_\psi = -k_\psi s_\psi. \quad (12)$$

With (3), (4), and (5a), the closed-loop height subsystem is

$$\dot{\vartheta}_{h1} = b_h k_h \vartheta_{h2} - (b_h k_h - \alpha_h) \vartheta_{h1} - \alpha_h^2 e_{sh} + b_h \tilde{C}_g \quad (13a)$$

$$\dot{\vartheta}_{h2} = b_h \tilde{C}_g - b_h k_h \vartheta_{h1} - (l_h - l_{hd} - b_h k_h) \vartheta_{h2} - l_{hd}^2 \tilde{e}_{sh} \quad (13b)$$

$$\dot{e}_{sh} = \vartheta_{h1} - \alpha_h e_{sh} \quad (13c)$$

$$\dot{\tilde{e}}_{sh} = \vartheta_{h2} - l_{hd} \tilde{e}_{sh} \quad (13d)$$

$$\dot{\tilde{C}}_g = -\gamma_h (\vartheta_{h1} + \vartheta_{h2}) \quad (13e)$$

with  $\tilde{C}_g = \hat{C}_g + C_{g0} - C_g$ . A Lyapunov function candidate for (13) is  $V_h = (\vartheta_{h1}^2 + \vartheta_{h2}^2 + \alpha_h^2 e_{sh}^2 + l_{hd}^2 \tilde{e}_{sh}^2 + b_h \tilde{C}_g^2 / \gamma_h) / 2$ , whose time derivative is  $\dot{V}_h = -(b_h k_h - \alpha_h) \vartheta_{h1}^2 - (l_h - l_{hd} - b_h k_h) \vartheta_{h2}^2 - \alpha_h^3 e_{sh}^2 - l_{hd}^3 \tilde{e}_{sh}^2$ . If the control gains  $\alpha_h$ ,  $k_h$ ,  $l_h$ , and  $l_{hd}$  satisfy (11), we have  $\dot{V}_h \leq 0$ . Hence, the closed loop is stable, which implies state  $x_h = [\vartheta_{h1}, \vartheta_{h2}, e_{sh}, \tilde{e}_{sh}, \tilde{C}_g]^T$  is bounded. Also, it is easy to show that equilibrium  $x_h = 0$  is the only invariant set in  $E = \{x_h \in \mathbb{R}^5 : \dot{V}_h(x_h) = 0\}$ . Hence, applying LaSalle's theorem, we can show the equilibrium  $x_h = 0$  of the closed loop (13) is AS. Since (13) is linear time-invariant, we have proven ES. As  $\vartheta_{h1}$  and  $e_{sh}$  are exponentially convergent, we can show  $\dot{e}_{sh}$  is ES. Hence, using (3), we conclude  $s_h - 1$  and  $v_3^v$  exponentially converge to zero.

With the control (4) and (8), the lateral subsystem (7) is

$$\ddot{s}_l = b_l k_l (\vartheta_{l2} - \vartheta_{l1}) + b_l \tilde{\Delta}_l + d_l(t) + B_{\eta 1}(t) e_{\eta 1} \quad (14)$$

where  $\tilde{\Delta}_l = \hat{\Delta}_l - \Delta_l$ ,  $e_{\eta 1} = \eta_1 - \eta_1^*$ ,  $B_{\eta 1}(t) = -u_h b_l S / C_g$ , and

$$d_l(t) = B_{ud}(x_l) u_d = B_{xl}(u_d) x_l + B_{\Delta} \tilde{u}_h \quad (15)$$

with  $B_{ud}(t) = [b_{ud1}, b_{ud2}, b_{ud3}, b_{ud4}]$ ,  $u_d = [\tilde{u}_h, \dot{\psi}^2, \dot{\psi}, \ddot{\psi}]^T$ ,  $\tilde{u}_h = u_h - C_g$ ,  $b_{ud1} = b_l(k_l(\vartheta_{l2} - \vartheta_{l1}) + \tilde{\Delta}_l + \Delta_l) / C_g$ ,  $b_{ud2} = e_{sl}$ ,  $b_{ud3} = 2S(\alpha_l e_{sl} - \vartheta_{l1})$ ,  $b_{ud4} = -S e_{sl}$ ,  $B_{xl}(t) = [B_{xl1}, B_{xl2}, B_{xl3}, 0, B_{xl5}]^T$ ,  $x_l = [\vartheta_{l1}^T, \vartheta_{l2}^T, e_{sl}^T, \tilde{e}_{sl}^T, \tilde{\Delta}_l^T]^T$ ,  $B_{xl1} = -b_l \tilde{u}_h k_l / C_g - 2S\dot{\psi}$ ,  $B_{xl2} = b_l \tilde{u}_h k_l I_2 / C_g$ ,  $B_{xl3} = 2\alpha_l S \dot{\psi} - S \ddot{\psi} + \psi^2 I_2$ ,  $B_{xl5} = -b_l \tilde{u}_h / C_g$ , and  $B_{\Delta} = b_l \Delta_l / C_g$ . With (10) and (12), we can write  $\psi(t) = s_{\psi 0}(1 - e^{-k_\psi t})$ , where  $s_{\psi 0}$  is the initial value of  $s_\psi$ . Hence,  $\dot{\psi}$  and  $\ddot{\psi}$  exponentially

converge to zero. The control (4) can be written as  $u_h = k_h(\vartheta_{h2} - \vartheta_{h1}) + \tilde{C}_g + C_g$ . As shown earlier, the error signals  $\vartheta_{h1}$ ,  $\vartheta_{h2}$ , and  $\tilde{C}_g$  exponentially converge to zero, therefore,  $\tilde{u}_h$  exponentially converges to zero. Thus, we conclude that  $u_d$  and  $B_{xl}$  exponentially converge to zero. With (9), (14), (15), and assuming the inner loop tracks its reference perfectly, the closed loop for the lateral subsystem is

$$\dot{x}_l = A_{cl} x_l + B_d u_d = A_{cl} x_l + B_l x_l + B_{\Delta l} \tilde{u}_h \quad (16)$$

where  $B_d = [B_{ud}^T, B_{ud}^T, 0, 0, 0]^T$ ,  $B_l = [B_{xl}^T, B_{xl}^T, 0, 0, 0]^T$ ,  $B_{\Delta l} = [B_{\Delta}^T, B_{\Delta}^T, 0, 0, 0]^T$ ,  $A_{cl} = A_l \otimes I_2$ , with  $\otimes$  denoting the Kronecker product operator, and

$$A_l = - \begin{bmatrix} (b_l k_l - \alpha_l) & -b_l k_l & \alpha_l^2 & 0 & -b_l \\ b_l k_l & (l_l - l_{ld} - b_l k_l) & 0 & l_{ld}^2 & -b_l \\ -1 & 0 & \alpha_l & 0 & 0 \\ 0 & -1 & 0 & l_{ld} & 0 \\ \gamma_l & \gamma_l & 0 & 0 & 0 \end{bmatrix}.$$

The structure of  $A_{cl} x_l$  is the same as the system matrix corresponding to (13). Hence, we conclude that if the control gains  $k_l$ ,  $l_l$ , and  $l_{ld}$  satisfy (11), the matrix  $A_{cl}$  is Hurwitz. Since  $A_{cl}$  is Hurwitz,  $B_l$  exponentially converges to zero,  $B_{\Delta l}$  is a constant matrix, and  $\tilde{u}_h$  exponentially converges to zero, we can show the trajectories of  $x_l$  are bounded using a converse Lyapunov theorem [28, Th. 4.14]. Since  $B_d$  is linear in  $x_l$ , we can also show the boundedness of  $B_d$ . Since  $u_d$  exponentially converges to zero and  $B_d$  is bounded, using [29, Lemma III.1], it can be shown that the origin of (16) is ES. From the definitions and exponential stability of  $\vartheta_{l1}$  and  $e_{sl}$ , we have shown  $s_l$  and  $v_l$  exponentially converge to zero.  $\square$

### C. Inner-Outer Loop Stability Analysis

In the previous section, the closed-loop lateral subsystem was proven ES for perfect inner loop tracking. In this section, we consider the effect of inner loop tracking error on the stability of the entire closed loop. There exists a rich literature on the stability analysis of cascaded-controlled UAVs, for example, [25] and [30]. In principle, if the bandwidth of the inner loop is sufficiently large, the entire closed loop is stable. To show this, the stability analysis is conducted by considering a simplified inner attitude dynamics. This simplification is practical as visual servoing is mainly about hover.

Using (14) and (16), the closed-loop of the outer loop can be written as

$$\dot{x}_l = A_{cl} x_l + B_d u_d + B_{e\eta} e_{\eta 1} \quad (17)$$

where  $B_{e\eta} = [B_{\eta 1}^T, B_{\eta 1}^T, 0, 0, 0]^T$ . With (8) and (17), the time derivative of  $\eta_{m1}^*$  is  $\dot{\eta}_{m1}^* = C_\eta A_{cl} x_l$ , where  $C_\eta = [-k_l S, k_l S, 0, 0, I_2]$ . As in [6], we take a linear approximation of (1e), (1f) about zero roll and pitch. The linearized inner loop is  $\dot{e}_{\eta 1} = \dot{\eta}_{m1} - \dot{\eta}_{m1}^*$  and  $\ddot{\eta}_{m1} = J_{12}^{-1} \tau_{12}^c$ , where we have assumed a diagonal inertia matrix with nonzero components  $J_i, i = 1, 2, 3$ ,  $J_{12} = \text{diag}([J_1, J_2])$ , and  $\tau_{12}^c$  is a vector of the first two components of  $\tau^c$ . We remark that the same practical justification for a small angle approximation is given as for (2). Defining  $\delta_1 = \int_0^t e_{\eta 1} d\tau$ ,  $\delta_2 = e_{\eta 1} / k_1 + \delta_1$ ,  $\delta_3 = \dot{\eta}_{m1} / k_2 + \delta_2$ ,

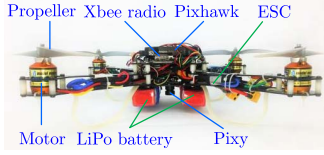


Fig. 3. Custom quadrotor UAV with visual servoing capability.

$x_\delta = [\delta_1^T, \delta_2^T, \delta_3^T]^T$ , and choosing the control  $\tau_{12}^c = -k_3\delta_3$ , we have

$$\dot{x}_\delta = A_\delta x_\delta - B_\delta x_l / k_1 \quad (18)$$

where

$$A_\delta = \begin{bmatrix} -k_1 I_2 & k_1 I_2 & 0 \\ -k_1 I_2 & -\frac{k_2 - k_1^2}{k_1} I_2 & \frac{k_2}{k_1} I_2 \\ -k_1 I_2 & -\frac{k_2 - k_1^2}{k_1} I_2 & -\frac{k_3}{k_2} J_{12}^{-1} + \frac{k_2}{k_1} I_2 \end{bmatrix}$$

and  $B_\delta = [0, A_{cl}^T C_\eta^T, A_{cl}^T C_\eta^T]^T$ . As shown earlier, the nominal system (16) of (17) is ES. Hence, we apply the converse Lyapunov theorem [28, Th. 4.14] which ensures there exists a function  $V_n(t, x_l)$  satisfying

$$c_1 \|x_l\|^2 \leq V_n(t, x_l) \leq c_2 \|x_l\|^2 \quad (19a)$$

$$\partial V_n / \partial t + \partial V_n / \partial t (A_{cl} x_l + B_d u_d) \leq -c_3 \|x_l\|^2 \quad (19b)$$

$$\|\partial V_n / \partial x_l\| \leq c_4 \|x_l\| \quad (19c)$$

for some positive constants  $c_i, i = 1, 2, 3$ , and 4. Considering a Lyapunov function candidate  $V = V_n(t, x_l) + x_\delta^T x_\delta / 2$  and with (18) and (19), we can show the time derivative of  $V$  satisfies  $\dot{V} \leq -c_3 \|x_l\|^2 + c_4 \|x_l\| \|B_{e\eta} e_{\eta 1}\| - x_l^T B_\delta x_\delta / k_1 + x_\delta^T (A_\delta^T + A_\delta) x_\delta / 2$ . We can choose appropriate gains  $k_i$  such that  $A_\delta^T + A_\delta = -Q_\delta$ , where  $Q_\delta > 0$ . Since  $B_{e\eta}, B_\delta$  are independent of gains  $k_i, i = 1, 2, 3$ ,  $e_{\eta 1}$  is linear in  $x_\delta$ , and applying Young's inequality, we can show that  $\dot{V} \leq -c_5 \|x_l\|^2$  for some constant  $c_5 > 0$ , where  $x_l = [x_l^T, x_\delta^T]^T$ , and if the eigenvalues of  $Q_\delta$  are taken sufficiently large. Hence, we conclude that if the bandwidth of the inner loop is sufficiently large, the entire closed-loop is ES. We remark that the control for the roll and pitch channels have a PID structure and can be written as

$$\tau_{12} = -k_3 \delta_3 = -k_3 \dot{\eta}_{m1} / k_2 - k_3 e_{\eta 1} / k_1 - k_3 \int_0^t e_{\eta 1} d\tau.$$

#### IV. EXPERIMENTAL RESULTS

##### A. Experimental Platform

To validate the proposed IBVS, a quadrotor platform shown in Fig. 3 was developed.

1) *Hardware*: The UAV is built on a generic carbon fiber frame and includes a CMUCam5 Pixy computer vision system<sup>1</sup> and the PX4v2 Pixhawk autopilot hardware.<sup>2</sup> The Pixhawk autopilot contains a 3-D accelerometer, a 3-D gyroscope, and a 3-D magnetometer. The Pixy camera is downward facing and mounted to the bottom of the vehicle. It has a focal length of  $\lambda = 2.8$  mm and a  $1/4''$  image sensor. The lens mounted on

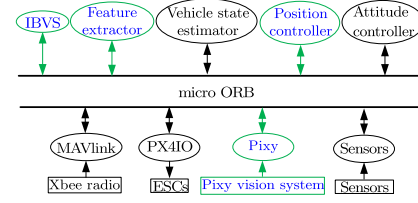


Fig. 4. Simplified PX4 autopilot software structure used for IBVS. Rectangles: data sources such as sensors or devices. Ovals: software modules.

the Pixy camera has  $75^\circ$  horizontal and  $47^\circ$  vertical FoV. The Pixy transmits image point coordinates at a rate of 25 Hz with a resolution of  $320 \times 200$  pixels. Four ESCs are used to control four 840-rpm/V brushless motors with  $10 \times 3.8''$  multirotor propellers. The arm length of the frame is  $l = 0.2$  m. Power is supplied by two 11.1-V 2600-mAh LiPo batteries. An Xbee radio provides a link to a Vicon capture system and is used for ground truth and for input to a backup controller for safety. The entire vehicle system weight including battery and computer vision system is about 1.2 kg.

2) *Software*: To test the proposed visual servoing algorithm, the open-source PX4 autopilot flight stack and device driver code were modified and developed. The PX4 autopilot runs on the real-time operating system NuttX<sup>3</sup> and has a modular structure which is enabled by a publish-subscribe interprocess communication microobject request broker ( $\mu$ ORB). Fig. 4 shows how the essential PX4 modules (i.e., applications) communicate through  $\mu$ ORB for the proposed control. Rectangles denote data sources such as sensors or devices, ovals denote software modules. For simplicity of presentation, not all components of the system are shown. A Pixy module was developed to receive the salient image point coordinates via a Universal Asynchronous Receiver/Transmitter interface. This module publishes this data to a topic called *pixy*. The module *feature extraction* subscribes to the *pixy* topic and computes the image moments and then publishes this data under the topic called *image\_features*. The visual servoing module (IBVS) subscribes to the *image\_features* topic and computes the reference attitude which is published for the *inner attitude controller* module. For safety (e.g., when the target leaves the FoV in IBVS), the existing *position control* module was modified to enable switching from visual servoing to position control using Vicon position and velocity data. The source code for the modified autopilot code has been released publicly<sup>4</sup> to encourage research collaboration.

##### B. Experimental Results

Although Theorem 1 guarantees the stability of the closed loop, the transient performance of the IBVS law needs to be adjusted by tuning its control gains in the experiment. Suitable transient performance ensures the visual target does not leave the camera FoV. Alternately, a camera with large FoV, e.g., a fisheye camera, could be used to avoid FoV problems. The values of the control gains for the outer loop are in Table I.

<sup>1</sup><http://www.cmucam.org/projects/cmucam5/wiki>

<sup>2</sup><https://pixhawk.org/>

<sup>3</sup><http://www.nuttx.org/>

<sup>4</sup><https://github.com/huixie-robot/VisualServoing>

TABLE I  
CONTROL GAINS

Gain	$k_h$	$\alpha_h$	$\gamma_h$	$l_h$	$l_{hd}$	$k_\psi$
Value	0.2	0.5	0.1	8.0	2.5	0.5
Gain	$k_l$	$\alpha_l$	$\gamma_l$	$l_l$	$l_{ld}$	
Value	0.08	0.125	0.04	4.0	1.0	

TABLE II  
STATISTICS OF  $e_s$ ,  $e_d$ , AND  $e_\psi$ 

Variable	mean	standard deviation
$e_{s1}$ (mm)	-0.01	0.01
$e_{s2}$ (mm)	0.09	0.02
$e_{s3}$	-0.02	0.01
$e_{s4}$ (rad)	0.00	0.01
$e_{d1}$ m	0.004	0.007
$e_{d2}$ (m)	-0.038	0.049
$e_{d3}$ (m)	0.015	0.004
$e_\psi$ (rad)	0.006	0.005

The constant estimate of  $C_g$  is  $C_{g0} = 0.5$ . The effectiveness of the proposed law to compensate for the uncertainty described in Section II is shown by comparing its performance to the case where the adaptive laws (5c) and (9c) are disabled. Such a comparison shows the need for modeling and compensating the system uncertainty considered. As well, the proposed method is compared to a PID control law obtained by removing the observer estimation error  $\tilde{e}_{sh}$ . This leads to a height control

$$u_h = -(k_h \alpha_h + \gamma_h) e_{sh} + k_h \hat{v}_h - \gamma_h \alpha_h \int_0^t e_{sh} d\zeta + C_{g0} \quad (20)$$

where  $\hat{v}_h$  is same as in (6) and obtained from filter (5a) and (5b). Similarly, for the lateral system, a PID controller-based visual servoing law can be obtained by removing the term  $\tilde{e}_{sl}$  in (8). The objective of the second comparison is to demonstrate the improved stability margin and ease of tuning of the proposed control relative to a PID law. To ensure a sensible comparison, all control gains for the three designs are taken the same.

The visual target consists of two points separated by about 0.36 m and located on the horizontal ground. The desired value of the image feature is  $s^* = [0, 0, 1, 0]^T$  with the desired height of the vehicle determining the expression for  $s_h$  [6]. The image feature error is denoted  $e_s = [e_{s1}, e_{s2}, e_{s3}, e_{s4}]^T = s - s^*$ . Fig. 5 shows the trajectories of  $e_s$  for the three cases. The trajectories of 3-D position and yaw tracking errors are denoted as  $e_t = [e_{t1}, e_{t2}, e_{t3}, e_{t4}]^T = t_{nc}^n - t_{nc}^{n*}$  and  $e_\psi = \psi - \psi^*$ , respectively, where  $t_{nc}^n$  and  $\psi^*$  correspond to the values of  $t_{nc}^n$  and  $\psi$  when  $e_s = 0$ . The Vicon system provides the ground truth  $t_{nc}^n$ . Fig. 6 shows the graphs of  $e_t$  and  $e_\psi$ . Fig. 7 presents the outer loop input trajectories, and Fig. 8 illustrates the estimates  $\hat{\Delta}_l = [\hat{\Delta}_{l1}, \hat{\Delta}_{l2}]^T$  and  $\hat{C}_g$  using the adaptive law (5c) and (9c). The trajectories of image points are given in Fig. 9.

As seen from Figs. 5(a) and 6(a), all error signals reach a steady state at about 10 s for the adaptive IBVS. The average and standard deviation of  $e_s$ ,  $e_t$ , and  $e_\psi$  after 10 s are given in Table II. The statistics of the steady-state error are similar to those in [6]. However, it is important to note that unlike [6]

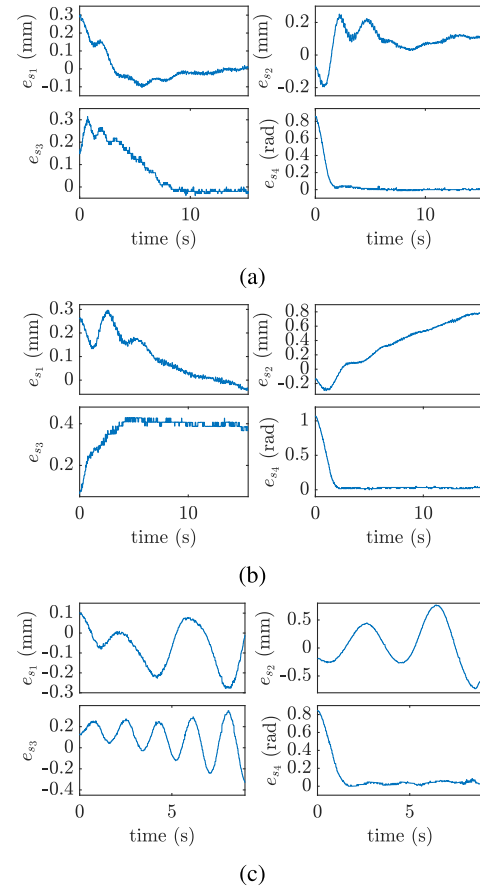


Fig. 5. Trajectories of image feature error  $e_s$ . (a) Proposed adaptive IBVS. (b) Nonadaptive IBVS. (c) PID IBVS.

velocity measurements from GPS or a motion capture system are not required. Figs. 5(b) and 6(b) show the error signal for the nonadaptive IBVS where uncertainty in  $K_T$  and  $\Delta$  are not compensated. We observe that feature error  $e_{s3}$  and vertical motion error  $e_{t3}$  reach their steady state at about 10 s but with significant steady-state error compared to the adaptive IBVS. This steady error comes from uncompensated positive  $C_{g0} - (mg + \Delta_3)/K_T$ . The steady-state error gradually decreases as  $K_T$  decreases. Because of the decreasing vehicle height and the inability to compensate  $\Delta_l$ , the lateral error signals  $e_{s1}$ ,  $e_{s2}$ ,  $e_{t1}$ , and  $e_{t2}$  vary slowly and monotonically. The monotonic variation in image feature error  $e_s$  in steady state is also seen in the image plane in Fig. 9(b). For the adaptive IBVS, the control signal  $u_h$  increases gradually to compensate decreases in  $K_T$ . This can be seen from Figs. 7(a) and 8 where the estimate of  $C_g - C_{g0}$  increases to compensate the decrease in  $K_T$ . The nonzero estimate of  $\Delta_l$  in Fig. 8 and almost zero steady error  $e_{s1}$ ,  $e_{s2}$  in Fig. 5(a) also show the importance of accounting for lateral additive disturbance arising from system uncertainties such as attitude bias. It can be readily shown analytically that the nonadaptive control has nonzero steady-state error independent of the choice of control gains and accuracy of the initial estimate  $C_{g0}$ . Although in theory, high control gains could reduce steady-state error, this is not feasible in practice due to

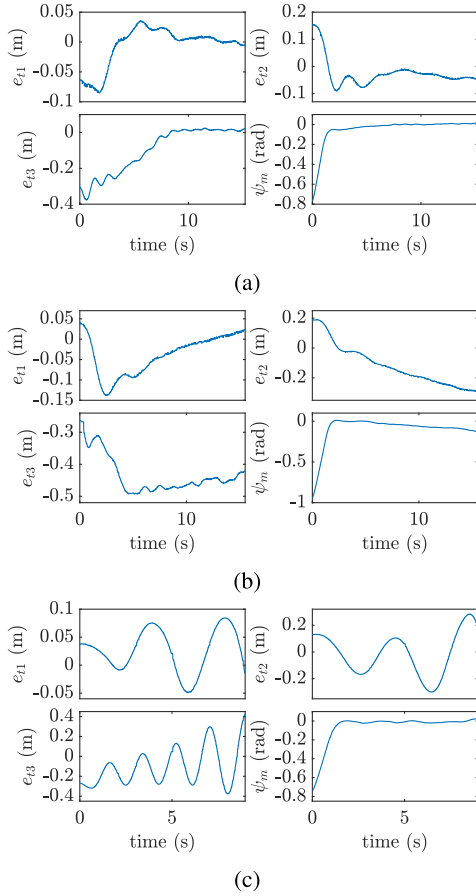


Fig. 6. 3-D position error  $e_t$  and yaw error  $e_{\psi}$ . (a) Proposed adaptive IBVS. (b) Nonadaptive IBVS. (c) PID IBVS.

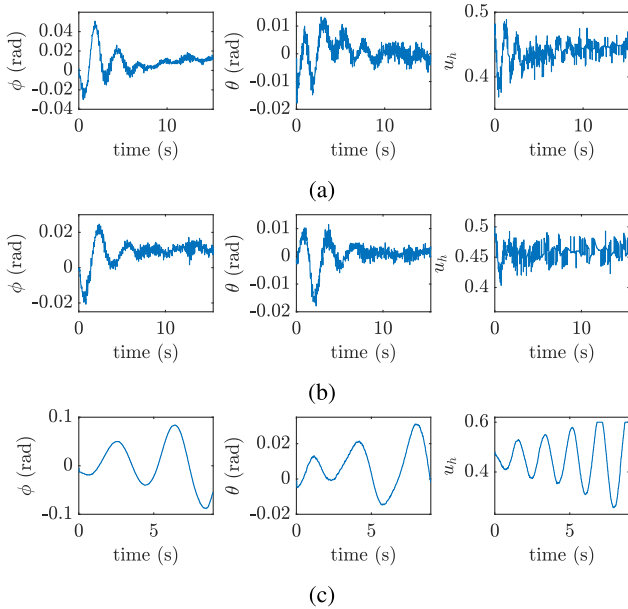


Fig. 7. Outer loop inputs. (a) Proposed adaptive IBVS. (b) Nonadaptive IBVS. (c) PID IBVS.

noisy image signals and the need to keep the target in the camera FoV.

It can be shown from Figs. 5(c)–7(c) and 9(c), the closed-loop system is unstable for the PID IBVS using the gains

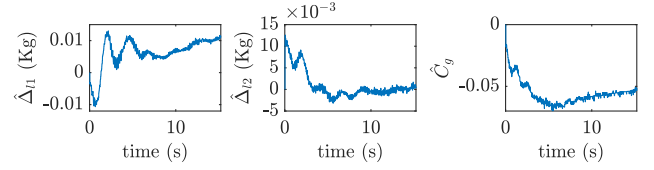


Fig. 8. Estimated parameters  $\hat{\Delta}_l$  and  $\hat{C}_g$ .

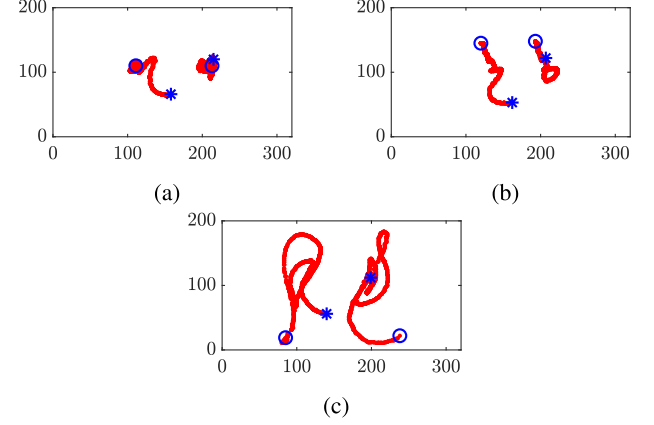


Fig. 9. Image points trajectories. (a) Proposed adaptive IBVS. (b) Nonadaptive IBVS. (c) PID IBVS.

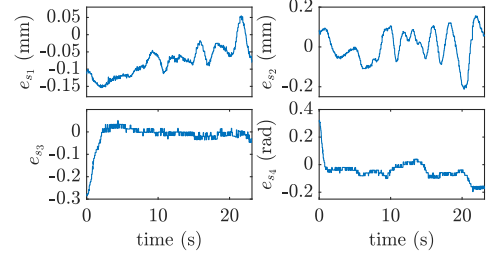


Fig. 10. Image feature error with a moving target.

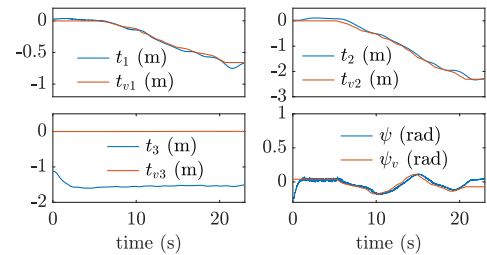


Fig. 11. Position and yaw of moving target and quadrotor. The target's 3-D position is denoted  $t_v^n = [t_{v1}, t_{v2}, t_{v3}]^T$  and yaw is denoted  $\psi_v$ .

in Table I. We speculate that it may be possible to tune the PID control law to stabilize the system. However, our experience has shown successful tuning is difficult in practice. This is possibly due to the fact that the calculation of the time derivative is inexact (i.e., a filter is used in the experiment). The gain of the observer cannot be chosen arbitrarily large due to noise in the image features, and thus the estimated time derivative of error signals is delayed, and this destabilizes the closed loop. On the other hand, we can easily tune the control parameters of the proposed control to stabilize the system. A simple rule is to choose small  $\alpha_h$ ,  $\alpha_l$  and large  $l_h - l_{hd}$ ,  $l_l - l_{ld}$  keeping  $k_h$ ,  $k_l$  fixed. Hence, the comparison isolates the role of the additional terms contained in the proposed control which is to clearly improve the stability margin of the system.



A video of the three experiments is available.<sup>5</sup> The proposed adaptive IBVS is shown to outperform the other designs.

Finally, a moving target experiment was considered. In Section III, the closed-loop system was proven to be ES for the case of a stationary target. When the target moves, its velocity acts as an additive disturbance to the closed loop. Using the converse Lyapunov stability theorem [28, Th. 4.14], we can show tracking error is bounded for bounded target acceleration. In this test, we dragged the target along the ground starting at about 8 s with a speed of approximately 0.25 m/s. The yaw of the target was also varied. The image feature error trajectories are shown in Fig. 10. As expected, the image feature errors remain bounded. Fig. 11 presents the 3-D position and yaw of the vehicle and target. It can be seen that the quadrotor successfully follows the target at a constant height of about 1.55 m.

## V. CONCLUSION

This brief presents an adaptive output feedback dynamic IBVS control which makes use of commonly found low-cost sensors: an inertial measurement unit and monocular computer vision system. The main benefit of output feedback is that it avoids directly measuring linear velocity or computing optical flow. An adaptive control method ensures robustness to constant force disturbances; and uncertainty in desired depth, mass, and thrust coefficient. This brief provides experimental results which show the proposed method accurately controls the relative pose of the vehicle to the horizontal target. In particular, steady-state performance is obtained as the method compensates for variation in thrust constant and constant bias in attitude measurement which is modeled by a constant force disturbance. Local exponential stability of the outer loop and the entire closed loop is proven. Future work focuses on time-varying external disturbances and incorporating attitude bounds to ensure the visual feature remains in the camera FoV [31]. Finally, improving the entire closed-loop stability analysis from a local to global result should be investigated.

## REFERENCES

- [1] S. M. Weiss, "Vision based navigation for micro helicopters," Ph.D. dissertation, Dept. Mech. Process Eng., ETH, Zürich, Switzerland, 2012.
- [2] S. Shen, "Autonomous navigation in complex indoor and outdoor environments with micro aerial vehicles," Ph.D. dissertation, Dept. Elect. Syst. Eng., Univ. Pennsylvania, Philadelphia, PA, USA, 2014.
- [3] F. Chaumette and S. Hutchinson, "Visual servo control. I: Basic approaches," *IEEE Robot. Automat. Mag.*, vol. 13, no. 4, pp. 82–90, Dec. 2006.
- [4] B. Espiau, "Effect of camera calibration errors on visual servoing in robotics," in *Experimental Robotics III*, vol. 200, T. Yoshikawa and F. Miyazaki, Eds. Berlin, Germany: Springer, 1994, pp. 182–192.
- [5] F. Chaumette and S. Hutchinson, "Visual servo control. II. Advanced approaches," *IEEE Robot. Autom. Mag.*, vol. 14, no. 1, pp. 109–118, Mar. 2007.
- [6] H. Xie, "Dynamic visual servoing of rotary wing unmanned aerial vehicles," Ph.D. dissertation, Dept. Elect. Comput. Eng., Univ. Alberta, Edmonton, AB, Canada, 2016.
- [7] T. Hamel and R. Mahony, "Visual servoing of an under-actuated dynamic rigid-body system: An image-based approach," *IEEE Trans. Robot. Autom.*, vol. 18, no. 2, pp. 187–198, Apr. 2002.
- [8] O. Bourquardez, R. Mahony, N. Guenard, F. Chaumette, T. Hamel, and L. Eck, "Image-based visual servo control of the translation kinematics of a quadrotor aerial vehicle," *IEEE Trans. Robot.*, vol. 25, no. 3, pp. 743–749, Jun. 2009.
- [9] N. Metni, T. Hamel, and F. Derkx, "Visual tracking control of aerial robotic systems with adaptive depth estimation," in *Proc. 44th IEEE Conf. Decis. Control*, Seville, Spain, Dec. 2005, pp. 6078–6084.
- [10] H. de Plinval, P. Morin, P. Mouyon, and T. Hamel, "Visual servoing for underactuated VTOL UAVs: A linear, homography-based framework," *Int. J. Robust Nonlinear control*, vol. 24, no. 16, pp. 2285–2308, Nov. 2014.
- [11] R. Ozawa and F. Chaumette, "Dynamic visual servoing with image moments for a quadrotor using a virtual spring approach," in *Proc. IEEE Int. Conf. Robot. Automat.*, Shanghai, China, May 2011, pp. 5670–5676.
- [12] R. Ozawa and F. Chaumette, "Dynamic visual servoing with image moments for an unmanned aerial vehicle using a virtual spring approach," *Adv. Robot.*, vol. 27, no. 9, pp. 683–696, Apr. 2013.
- [13] D. Lee, H. Lim, H. J. Kim, Y. Kim, and K. J. Seong, "Adaptive image-based visual servoing for an underactuated quadrotor system," *J. Guid., Control, Dyn.*, vol. 35, no. 4, pp. 1335–1353, Jul. 2012.
- [14] H. Jabbari, G. Oriolo, and H. Bolandi, "An adaptive scheme for image-based visual servoing of an underactuated UAV," *Int. J. Robot. Autom.*, vol. 29, no. 1, pp. 92–104, Jan. 2014.
- [15] R. Mahony, P. Corke, and T. Hamel, "Dynamic image-based visual servo control using centroid and optic flow features," *J. Dyn. Syst., Meas., Control*, vol. 130, no. 1, Jan. 2007, Art. no. 011005.
- [16] F. Le Bras, R. Mahony, T. Hamel, and P. Binetti, "Dynamic image-based visual servo control for an aerial robot: Theory and experiments," *Int. J. Optomechatron.*, vol. 2, no. 3, pp. 296–325, Jul. 2008.
- [17] B. Herissé, T. Hamel, R. Mahony, and F.-X. Russotto, "Landing a VTOL unmanned aerial vehicle on a moving platform using optical flow," *IEEE Trans. Robot.*, vol. 28, no. 1, pp. 77–89, Feb. 2012.
- [18] R. Mebarki and B. Siciliano, "Velocity-free image-based control of unmanned aerial vehicles," in *Proc. IEEE/ASME Int. Conf. Adv. Intell. Mechatronics*, Jul. 2013, pp. 1522–1527.
- [19] R. Mebarki, V. Lippiello, and B. Siciliano, "Nonlinear visual control of unmanned aerial vehicles in GPS-denied environments," *IEEE Trans. Robot.*, vol. 31, no. 4, pp. 1004–1017, Aug. 2015.
- [20] F. Le Bras, T. Hamel, R. Mahony, and A. Treil, "Output feedback observation and control for visual servoing of VTOL UAVs," *Int. J. Robust Nonlinear Control*, vol. 21, no. 9, pp. 1008–1030, Jun. 2011.
- [21] O. Tahri and F. Chaumette, "Point-based and region-based image moments for visual servoing of planar objects," *IEEE Trans. Robot.*, vol. 21, no. 6, pp. 1116–1127, Dec. 2005.
- [22] H. J. Asl, G. Oriolo, and H. Bolandi, "Output feedback image-based visual servoing control of an underactuated unmanned aerial vehicle," *Proc. Inst. Mech. Eng. I, J. Syst. Control Eng.*, vol. 228, no. 7, pp. 435–448, May 2014.
- [23] D. Zheng, H. Wang, J. Wang, S. Chen, W. Chen, and X. Liang, "Image-based visual servoing of a quadrotor using virtual camera approach," *IEEE/ASME Trans. Mechatronics*, vol. 22, no. 2, pp. 972–982, Apr. 2017.
- [24] H. Xie, K. H. Low, and Z. He, "Adaptive visual servoing of unmanned aerial vehicles in GPS-denied environments," *IEEE/ASME Trans. Mechatronics*, vol. 22, no. 6, pp. 2554–2563, Dec. 2017.
- [25] A. Abdessameud and F. Janabi-Sharifi, "Image-based tracking control of VTOL unmanned aerial vehicles," *Automatica*, vol. 53, pp. 111–119, Mar. 2015.
- [26] P. Castillo, R. Lozano, and A. E. Dzul, *Modelling and Control of Mini-Flying Machines*. London, U.K.: Springer, 2005.
- [27] H. Berghuis and H. Nijmeijer, "Robust control of robots via linear estimated state feedback," *IEEE Trans. Autom. Control*, vol. 39, no. 10, pp. 2159–2162, Oct. 1994.
- [28] H. K. Khalil, *Nonlinear Systems*, 3rd ed. Upper Saddle River, NJ, USA: Prentice-Hall, 2001.
- [29] R. Marino and P. Tomei, "Adaptive observers with arbitrary exponential rate of convergence for nonlinear systems," *IEEE Trans. Autom. Control*, vol. 40, no. 7, pp. 1300–1304, Jul. 1995.
- [30] Y. Yu and X. Ding, "A global tracking controller for underactuated aerial vehicles: Design, analysis, and experimental tests on quadrotor," *IEEE/ASME Trans. Mechatronics*, vol. 21, no. 5, pp. 2499–2511, Oct. 2016.
- [31] H. Xie and A. F. Lynch, "Input saturated visual servoing for unmanned aerial vehicles," *IEEE/ASME Trans. Mechatronics*, vol. 22, no. 2, pp. 952–960, Apr. 2017.

<sup>5</sup><https://youtu.be/tCA2oNs-5mI>